

RESEARCH

Open Access



Experimental Study on Spall Resistance of Steel-Fiber Reinforced Concrete Slab Subjected to Explosion

Dapeng Yang¹, Bei Zhang^{2*} and Guojun Liu¹

Abstract

Steel-fiber reinforced concrete slabs have good blast and spall resistance. In this study, compression and splitting tensile experiments were carried out to obtain the basic quasi-static mechanical properties of the steel-fiber concrete specimens and the influence of steel-fiber parameters was revealed. In-field explosion experiments were performed to study the dynamic responses and damage modes of the steel-fiber reinforced concrete slabs. Five typical spall damage modes were observed, the distribution law of the spalling fragments was obtained, and the influence of steel-fiber shape, length, length–diameter ratio and volume percentage on the spall performance were revealed. These results will provide a basis for the application of steel-fiber reinforced concrete slabs in protective structures.

Keywords: steel-fiber reinforced concrete slab, explosion test, steel-fiber parameters, spall damage

1 Introduction

With the development of high-tech weapon technology, the improvement of the structure's anti-blast performance has received a lot of attention. Many scholars use new materials and new structural forms to improve the anti-blast performance of the structure. Fan HL et al. (Zhang et al., 2019; Zhao et al., 2018) has conducted experiments and theoretical analysis on different type all-composite protective panels, which can improve explosion resistance while keeping lightweight. Wanchoo et al. (2021) made a comprehensive analysis of the mitigation effect of polymer composite structure on air and underwater explosions. Gunaryo et al. (2020) conducted experiments and numerical simulations on the response of glass/epoxy composite glass panels under blast impact loading. There are also many studies on the optimization of traditional concrete structures, such as mixing different fibers in concrete (Han et al., 2019; Nam et al., 2017;

Zhang et al., 2020) and wrapping fiber cloth on the surface of the structure (Jahami et al., 2019).

Steel-fiber concrete refers to a kind of composite cement-based material formed by mixing irregularly distributed steel-fibers into ordinary concrete (Michels et al., 2013). Since the beginning of the last century, American scholar Poter (1910) has proposed the concept of steel-fiber concrete, scholars from all over the world have carried out related research on the steel-fiber concrete and made great progress and breakthroughs (Pros et al., 2012; Rambo et al., 2014; Saboori et al., 1976; Thomas & Ramaswamy, 2007; Tokgoz & Dundar, 2010). Nataraja et al. (1999), Uygunoğlu (2008), and Lee et al. (2017) analyzed the mechanical properties of steel-fiber concrete in compression, bending and shearing, respectively. As an important means of concrete modification, compared with ordinary concrete, steel-fiber concrete indicated much higher tensile strength and fracture energy (Chanh, 2017; Yang et al., 2017). It can not only inhibit the early plastic cracks in concrete, but also control the expansion of concrete cracks under external force, greatly improving the tensile and bending resistance, and impact resistance of concrete. Behbahani and

*Correspondence: zhangbei_qd@163.com

² Institute of Defense Engineering, AMS, PLA, Beijing 100850, China
Full list of author information is available at the end of the article
Journal information: ISSN 1976-0485 / eISSN 2234-1315

Table 1 The design and preparation scheme of steel-fiber concrete specimens.

No.	Parameters of steel-fiber				Remarks
	Volume percentage (%)	Shape	Length (mm)	Length–diameter ratio	
FC00	–	–	–	–	Ordinary concrete
FC01	1.5	Hook-end shape	32	60	Shape contrast
FC02	1.5	Corrugated shape	32	60	
FC03	1.5	Dumbbell shape	32	60	
FC04	1.5	Hook-end shape	32	60	Length contrast
FC05	1.5	Hook-end shape	45	60	
FC06	1.5	Hook-end shape	50	60	
FC07	1.5	Hook-end shape	45	40	Length–diameter ratio contrast
FC08	1.5	Hook-end shape	45	60	
FC09	1.5	Hook-end shape	45	80	
FC10	1.0	Hook-end shape	45	60	Volume percentage contrast
FC11	2.0	Hook-end shape	45	60	
FC12	3.0	Hook-end shape	45	60	

Nematollahi (2011) made a detailed summary of the mechanical properties and impact resistance of steel-fiber concrete at that time.

Steel-fiber reinforced concrete refers to steel-fiber concrete with steel bars arranged according to reinforcement ratio. Many scholars have conducted experimental research on the anti-explosion performance of different steel-fiber reinforced concrete structures (Aoude et al., 2015; Li et al., 2015a; Luccioni et al., 2017; Yi et al., 2012), such as columns (Burrell et al., 2014; Xu et al., 2016), walls (Li et al., 2014), and slabs (Li et al., 2016, 2017; Mao et al., 2014). Others have performed numerical simulation analysis on the anti-explosion of steel-fiber reinforced concrete (Fang & Zhang, 2013; Li et al., 2015b). Yoo and Yoon (2016) made a detailed analysis on the structural behavior, design and application of ultra-high performance fiber-reinforced concrete. According to research, the traditional reinforced concrete structure has good anti-explosion ability. However, under the action of contact explosion, the explosion shock wave is transmitted to the back surface to form a reflection tensile wave, which causes serious spall damage on the back surface, which is the main failure mode of reinforced concrete structures (Chen et al., 2014, 2015; Feng et al., 2017; Liu et al., 2019; Wang et al., 2018, 2019; Xie et al., 2014). Research data at home and abroad have shown that steel-fiber reinforced concrete has a good ability to resist local spall damage caused by explosion. But this kind of spall damage phenomenon involves complex stress wave propagation, material response inside the reinforced concrete structure and other problems, so it is necessary to study the anti-spall mechanism of large size steel-fiber reinforced concrete m slabs.

Table 2 The physical and mechanical properties of cement.

Stability	Initial setting time (min)	Final setting time (min)	3d flexural strength (MPa)	3d compressive strength (MPa)
Qualified	200	255	5.1	26.9

In this paper, contact explosion tests were performed on steel-fiber reinforced concrete slabs with different steel-fiber shapes, lengths, length–diameter ratios and volume percentages. The influence of steel-fiber parameters on the spall resistance of slabs was systematically studied, which provided a basis for the practical application of steel-fiber reinforced concrete slabs in the protective structure.

2 Static Test

The static test can examine the basic mechanical properties of steel-fiber concrete and provide basis for the in-field explosion test. For the comparative test, 12 kinds of steel-fiber concrete specimens were designed and prepared, as listed in Table 1. The steel-fiber concrete used P.O42.5 ordinary Portland cement, and its physical and mechanical properties are listed in Table 2. The mix proportion of steel-fiber concrete is listed in Table 3. The parameters of steel fiber are listed in Table 4. The steel-fiber concrete used three different shapes of steel fiber, which were hook-end shape, corrugated shape, and dumbbell shape, respectively, as shown in Fig. 1. The longitudinal direction of the hook-shaped steel fiber is straight with hooks at both ends, and the surface is smooth. The surface of

Table 3 The mix proportion of steel-fiber concrete.

Cement (kg/m ³)	Simicon fume (kg/m ³)	Fly ash (kg/m ³)	Fine aggregate (kg/m ³)	Coarse aggregate (kg/m ³)	Water–binder ratio (kg/m ³)	Water reducing agent (kg/m ³)
373	80	80	828	828	0.29	3.7

Table 4 The parameters of steel fiber.

No.	Shape	Length (mm)	Equivalent diameter (mm)	Length–diameter ratio	Tensile strength (MPa)
1	Corrugated shape	32	0.53	60	1200
2	Dumbbell shape	32	0.53	60	900
3	Hook-end shape	45	0.75	60	1000
4	Hook-end shape	32	0.53	60	1000
5	Hook-end shape	50	0.83	60	1000
6	Hook-end shape	45	1.13	40	1000
7	Hook-end shape	45	0.56	80	1000

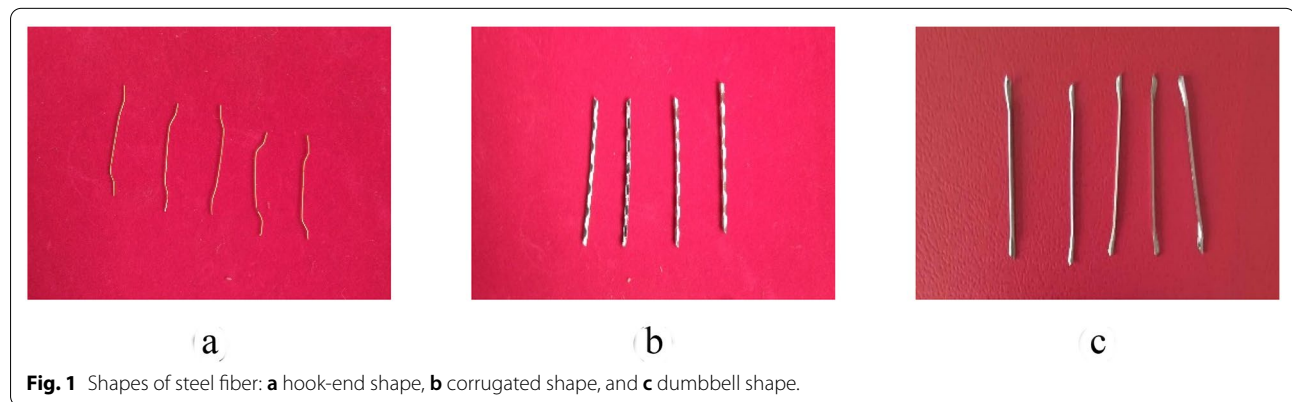


Fig. 1 Shapes of steel fiber: **a** hook-end shape, **b** corrugated shape, and **c** dumbbell shape.

the corrugated steel fiber has fine and dense indentations. The surface of the dumbbell-shaped steel fiber is also smooth, with dumbbell shapes at both ends. The lengths of steel fiber were 32 cm, 45 cm, and 50 cm. The length–diameter ratios of steel fiber were 40, 60, and 80. The volume percentage of steel fiber were 1.0%, 2.0%, and 3.0%. As listed in Table 1, FC00 is ordinary concrete specimen, FC04 and FC01 have the same steel-fiber parameters, and FC08 and FC05 have the same steel-fiber parameters. Each test specimen used a 150 mm × 150 mm × 150 mm cube standard specimen of steel-fiber concrete. There were 6 specimens in each working condition, 3 of which were used to compression test, and the other 3 specimens were used to splitting tensile strength test. The average value of the three measured results was taken as the final test result,

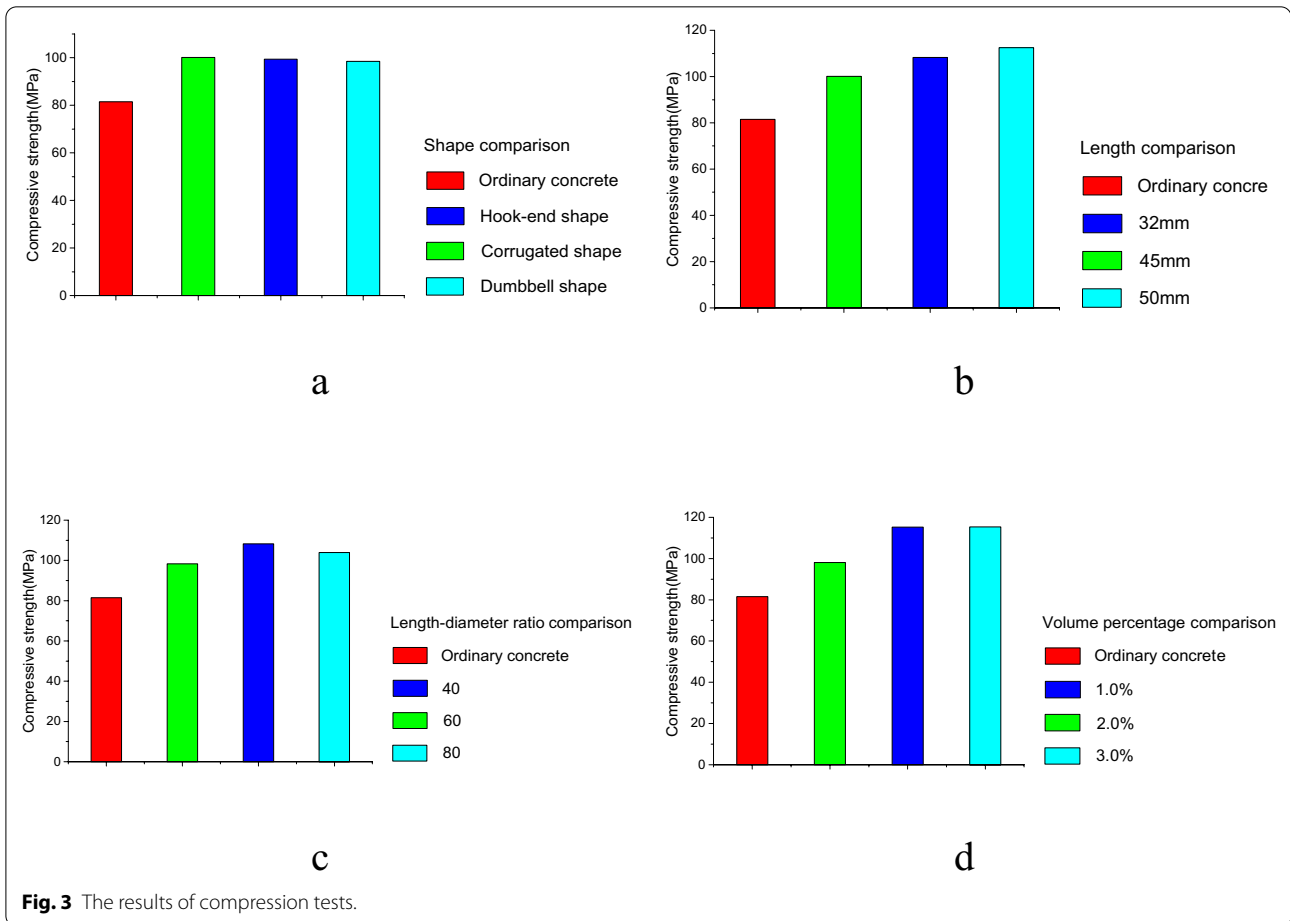
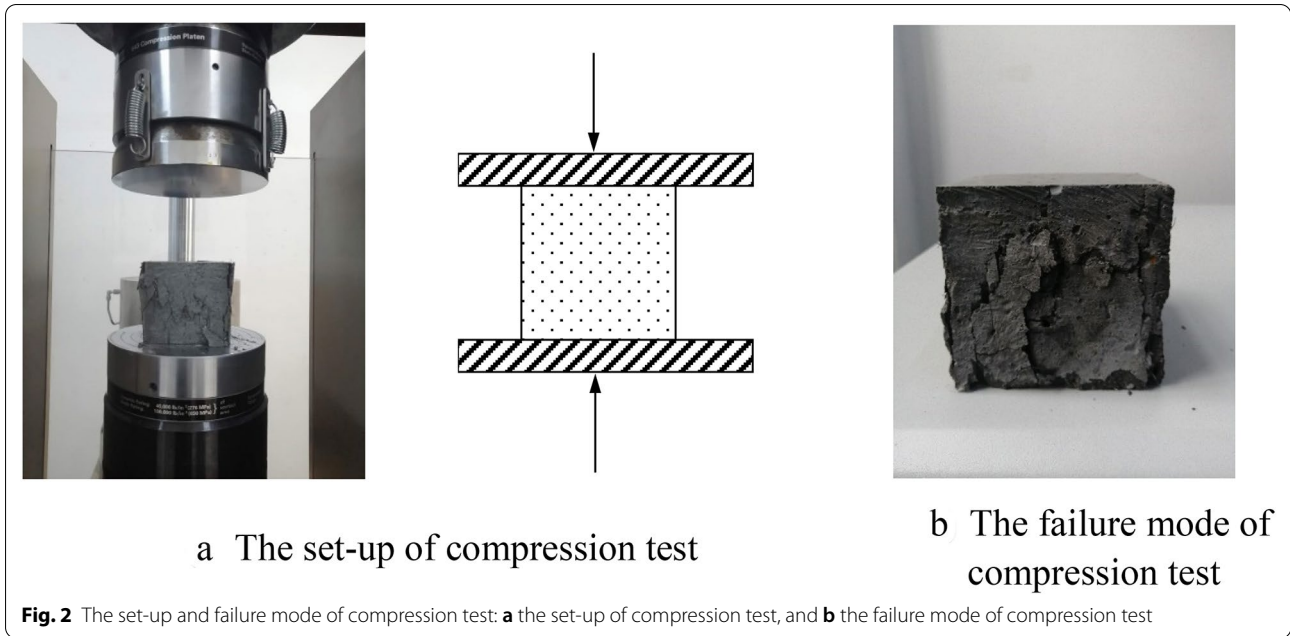
which provided basic mechanical parameters for subsequent tests and calculations.

The compression test and the splitting tensile test were performed, respectively. The set-up and failure mode of compression test is shown in Fig. 2. The cubic compressive strength of steel-fiber concrete f_c is calculated by

$$f_c = \frac{F_c}{A}, \tag{1}$$

where F_c is the compressive damage load, N , and A is the bearing area of test specimen, mm².

The cubic compressive strength of ordinary concrete is 81.5 MPa, and the comparison of compressive strength with different steel-fiber parameters is shown in Fig. 3. It can be shown that after adding steel fibers, the compressive strength of concrete has increased, but it is not



obvious. When the other parameters are the same, only the shape of the steel fibers is different, the compressive strength of steel-fiber concrete is basically equal, with an increase of between 20 and 23%, as shown in Fig. 3a. Except for the shape comparison, the hook-end steel fiber is used for all other working conditions. When the volume percentage and the length–diameter ratio are the same, the compressive strength increases as the length of the steel fiber increases, as shown in Fig. 3b. As shown in Fig. 3c, when the volume percentage and the length are the same, the steel-fiber concrete with the length–diameter ratio of 60 has the highest compressive strength, followed by the length–diameter ratio of 80, and the ratio of 40 is the worst. Therefore, simply increasing the length–diameter ratio does not improve the compressive strength of concrete. Under the same conditions, when the volume percentage of steel fiber is 1%, the compressive strength of the concrete is increased by 20.37%, and when the volume percentage is 2%, the compressive strength is increased by 41.59%, but as the volume percentage continues to increase to 3%, the compressive strength is not increased any longer, as shown in Fig. 3d.

The set-up and failure mode of splitting tensile strength test can be shown in Fig. 4. The splitting tensile strength of steel-fiber concrete f_t is calculated by

$$f_t = \frac{2F_t}{\pi A}, \tag{2}$$

where F_t is tensile damage load, N .

The results of splitting tensile strength tests can be shown in Fig. 5. The splitting tensile strength of ordinary concrete

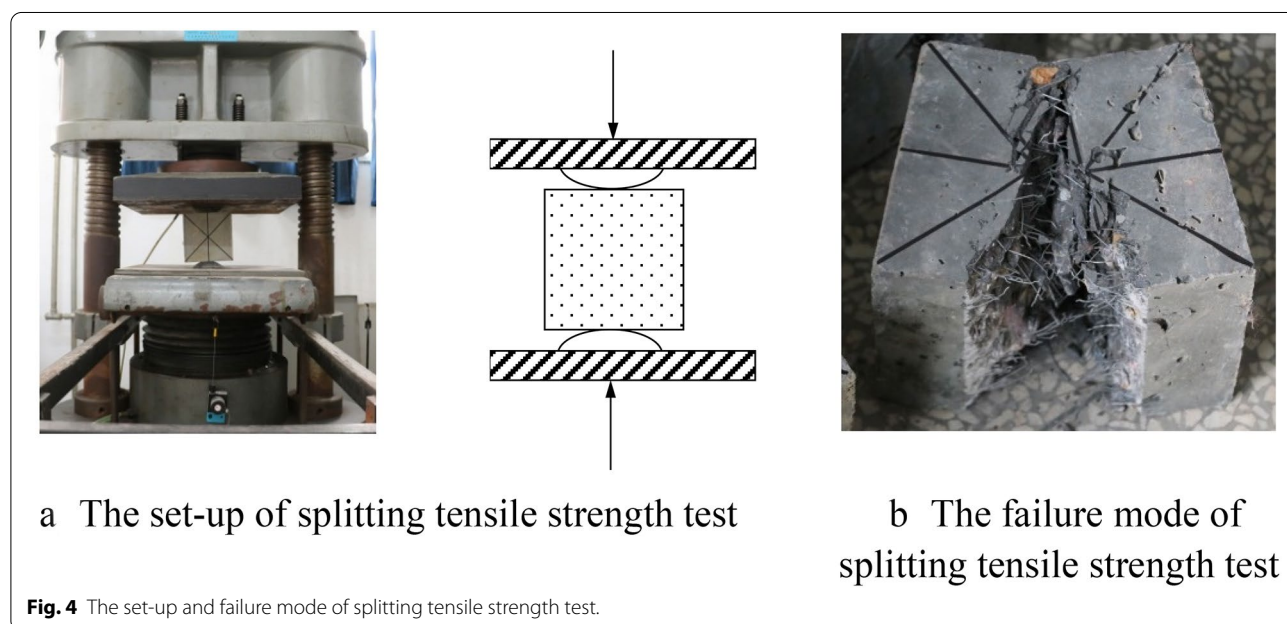
is 4.96 MPa. When other parameters are the same, the hook-end steel fiber has the largest influence on the splitting tensile strength, with an increase in tensile strength of 87.7%, followed by the tensile strength of the corrugated steel-fiber concrete, and the lowest tensile strength of dumbbell steel-fiber concrete.

When the hook-end steel fiber is used, the splitting tensile strength decreases with the increase of the length of the steel fiber, and increases with the increase of the length–diameter ratio and the volume percentage. Steel-fiber concrete with a volume percentage of 3% has a splitting tensile strength of 124.6% higher than that of ordinary concrete. It is obvious that the influence of steel fiber on splitting tensile strength is very significant.

It can be found that the influence of steel-fiber parameters on compressive strength and tensile strength is different. The influence of steel fiber on splitting tensile strength is related to shape, length l_f , diameter d_f , length–diameter ratio p , and volume percentage η . l_f , d_f , and p have the following relationship:

$$p = \frac{l_f}{d_f}. \tag{3}$$

As can be seen from Fig. 5, the tensile strength is approximately proportional to the length–diameter ratio and the volume percentage, and is inversely proportional to the length. According to this, it can be assumed that the splitting tensile strength, f_t is calculated by the following equation:



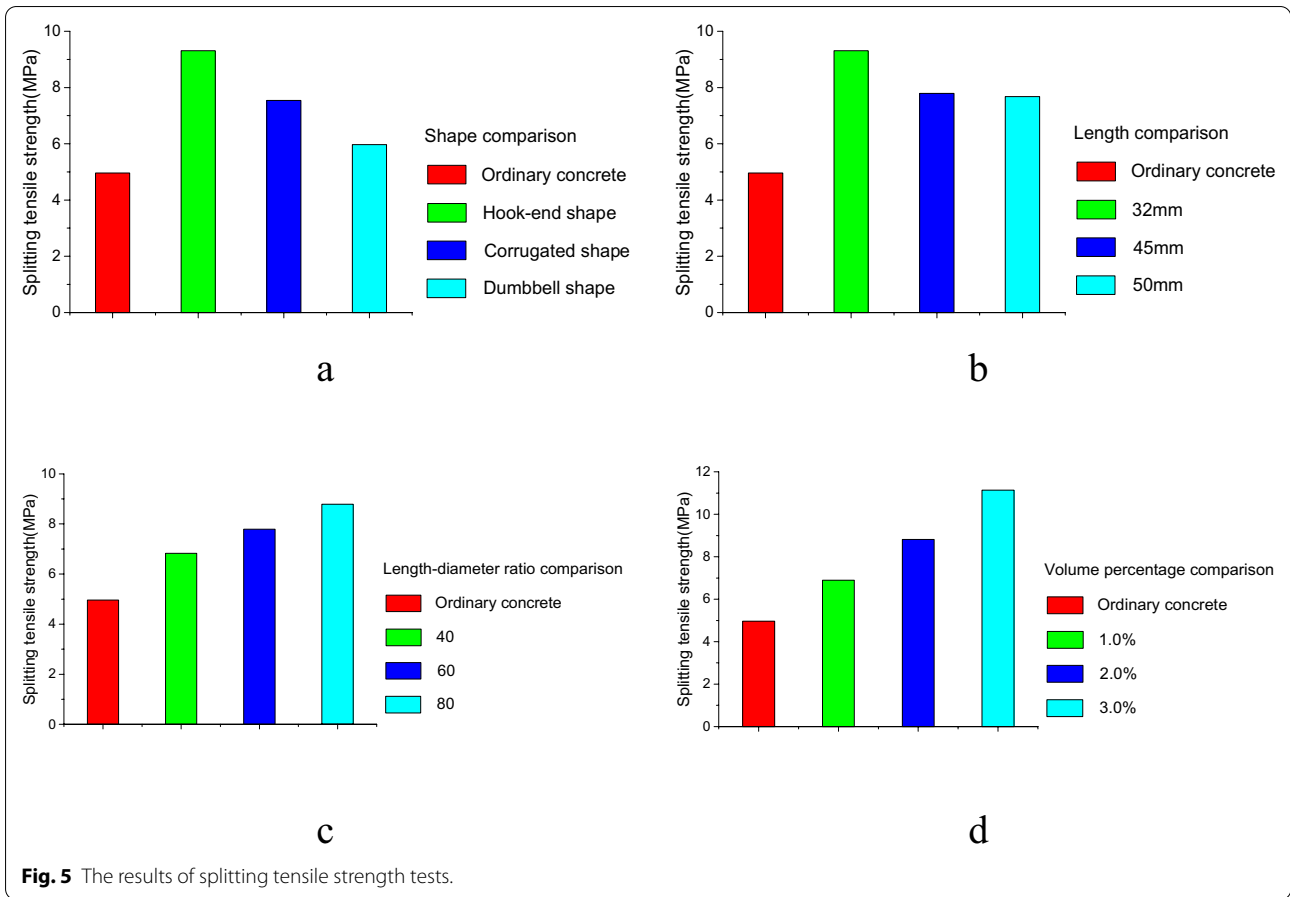


Fig. 5 The results of splitting tensile strength tests.

$$f_t = f_{ct} \left(1 + \frac{\alpha_t \eta p}{l_f} \right), \tag{4}$$

where f_{ct} is the splitting tensile strength of the concrete matrix, MPa, and α_t is the shape influence coefficient of steel fiber.

According to Eq. (4),

$$\alpha_t = \left(\frac{f_t}{f_{ct}} - 1 \right) / \frac{\eta p}{l_f}. \tag{5}$$

By nonlinearly fitting the test data, the shape influence coefficient of hook-end shaped steel-fiber concrete can be obtained as $\alpha_t = 0.029$. The splitting tensile strength of the hook-end shaped steel-fiber concrete can be further calculated by

$$f_t = f_{ct} \left(1 + 0.029 \frac{\eta p}{l_f} \right). \tag{6}$$

The applicable range of Eq. (6) is: $\eta \leq 3\%$, $40 \leq p \leq 80$, $30 \leq l_f \leq 50$.

Comparing the calculation with the experimental results, the relative error is within 5%, indicating that the fitting result is reasonable and feasible.

3 In-Field Explosion Experiments

In order to verify the spall resistance of the steel-fiber reinforced concrete slabs, the contact explosion test was carried out. The test mainly studies two aspects: one is the influence of steel-fiber parameters on the spall; the other is the anti-spall verification of steel-fiber reinforced concrete slabs.

The size of the steel-fiber reinforced concrete slab is $2 \text{ m} \times 2 \text{ m} \times 0.4 \text{ m}$. The slabs adopt double-layer reinforcement, the spacing between the two layers of steel bars is 0.3 m, and the spacing of the same layer of steel bars is $0.1 \text{ m} \times 0.1 \text{ m}$. The stressed steel bar is made of $\Phi 12 \text{ mm}$ HRB335 grade rebar, and the tie bar is made of $\Phi 6 \text{ mm}$ HRB335 grade rebar. The thickness of the protective layer of the steel is 40 mm. The reinforcement of the steel-fiber reinforced concrete slab is shown in Fig. 6.

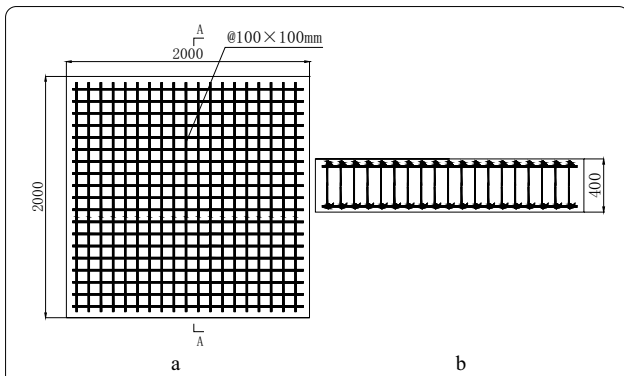


Fig. 6 The reinforcement of the steel-fiber reinforced concrete slab: **a** front view of slab. **b** Sectional view of A–A.

The test was divided into two steps. At first, three slabs were prepared for each working condition according to Table 1, and blasted by three different TNT charges. The purpose of this is to study the influence of steel-fiber parameters on the anti-spall performance. z is defined as the distance from the midpoint of the TNT to the midpoint on the back surface, m is defined as the mass of TNT, then the scaled distance on the back surface x can be expressed as:

$$x = \frac{z}{\sqrt[3]{m}} \tag{7}$$

The charges of three slabs in each working condition was 3.6 kg, 6.3 kg, and 9.6 kg, and the corresponding scaled distances x were $0.302 \text{ m/kg}^{1/3}$, $0.257 \text{ m/kg}^{1/3}$, and $0.229 \text{ m/kg}^{1/3}$, respectively.

To further verify the anti-spall performance of steel-fiber reinforced concrete slabs, four identical slabs were prepared according to FC05, and 4 explosion tests with different charges were carried out. The charges of four slabs were 2.5 kg, 3.0 kg, 4.5 kg, and 7.2 kg, and the corresponding scaled distances on the back surface were $0.331 \text{ m/kg}^{1/3}$, $0.321 \text{ m/kg}^{1/3}$, $0.280 \text{ m/kg}^{1/3}$, and $0.246 \text{ m/kg}^{1/3}$, respectively. Combined with the first-step tests, it can be considered that FC05 slabs have been subjected to 7 explosion tests with different TNT charges.

The area of the explosion test was a flat field of 20 m in length and 10 m in width, and a layer of 10-cm-thick sand was placed on the ground. The prefabricated test support was placed on one side of the test site, and the steel-fiber reinforced concrete slab was hoisted to the test support, as shown in Fig. 7. In order to prevent the fragments from scattering due to spall, a bamboo frame with a height of 3 m was placed around the test site, to capture the hit position when the pieces were scattered.

The measurement contents of the explosion test mainly include: pressure, steel strain, macroscopic failure mode and characteristics of spalled fragments. The measuring points of the pressure sensor and strain gauge were arranged as shown in Fig. 8. Four pressure sensors were

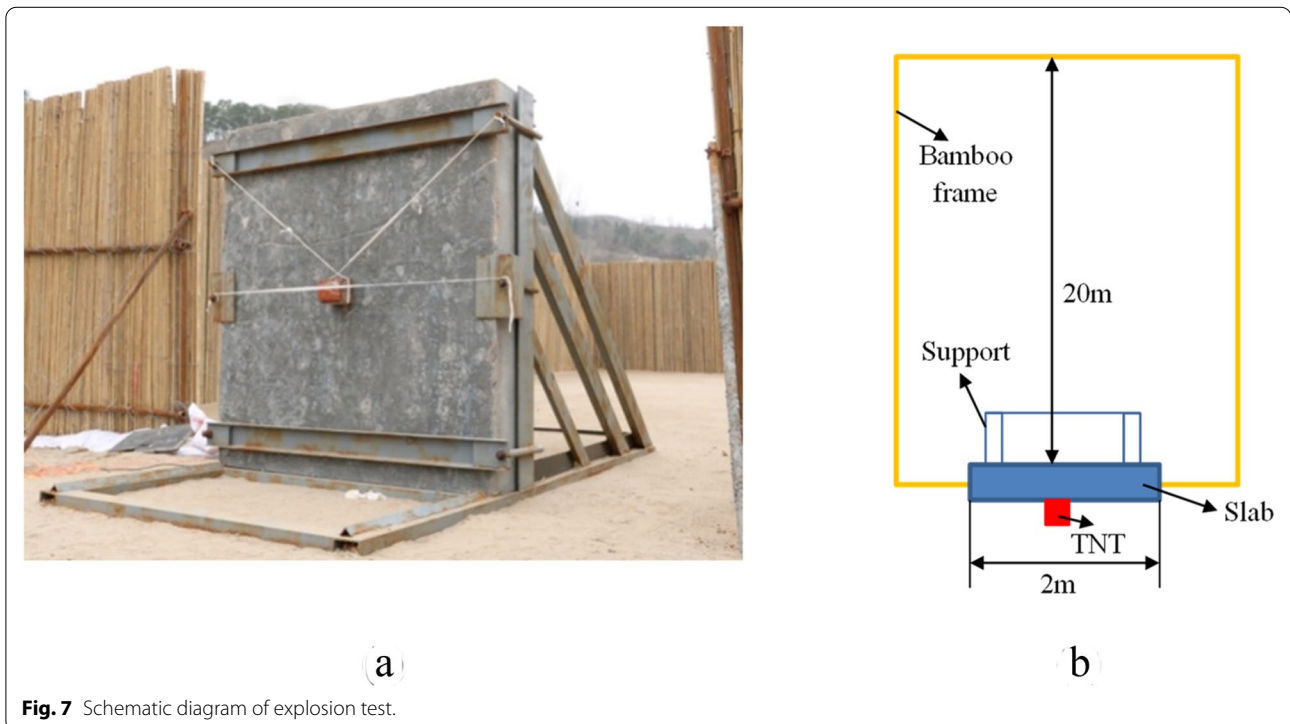
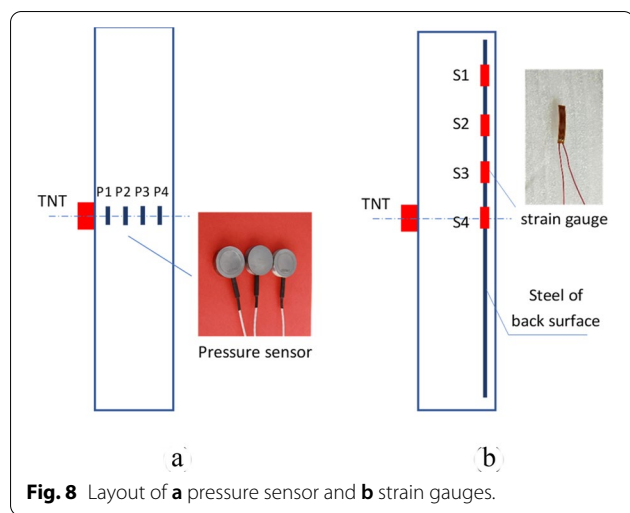


Fig. 7 Schematic diagram of explosion test.



fixed on the steel bar of the center line with a distance of 100 mm, and the test surface of the sensors faced the TNT. The pressure sensor was a piezoresistive sensor, the range of the sensor was 500 MPa, and the sampling frequency was 60 kHz. Four strain gauges were arranged on the steel of back surface, and the distance was 150 mm.

4 Experimental Analyses

4.1 Structural Response: Pressures and Strains

Pressure and strain time history curves can reflect the dynamic response and failure of the structure. The test results of FC05 slabs were taken as an example to describe the phenomenon of dynamic response, as shown in Fig. 9. It should be noted that the history curve only selects the data of the incident phase of the shock wave, because the sensors are destroyed in the subsequent stage. Figure 9a is the pressure time history curve of FC05 under 4.5 kg explosion. Since the P1 is too close to the TNT, the data have not been measured, and only the other three pressure points have been measured. The pressure peaks of P2, P3, and P4 are 261.5 MPa, 148.9 MPa, and 57.12 MPa, respectively. The pressure peak decays approximately linearly with increasing distance. Figure 9b is the pressure peak of the FC05 slab when the explosives are 4.5 kg, 6.3 kg and 9.6 kg, respectively. Figure 9c is the strain time history curve under 4.5 kg explosion. Subjected to explosive loadings, the slabs are tensioned and then compressed. The strain peak gradually decreases as the distance from center line increases. The trend of strain peak is shown in Fig. 9d.

Combined with the damage mode, the pressure and strain time history curves can reflect the typical failure process of the slab to some extent. In the test, TNT exploded at the top center of the slab. After the detonation process, the frontal surface of the slab was deformed

first. Under the action of high temperature and high pressure, the slab began to compress and formed a blasting crater. The steel-fiber concrete at the edge of the crater was mainly caused by compression-shear damage. Combined with the compression damage directly under the TNT, the blasting crater was further enlarged, and finally a funnel-shaped blasting crater was formed. After that, the explosion compression wave propagated and diffused further in the slab, and the pressure drops rapidly. When the pressure peak is less than the dynamic compressive strength of the steel-fiber concrete, the crater size no longer increased, and the slab only underwent plastic deformation.

When the compression wave propagated to the back surface of the slab, a reflected tensile wave was formed and propagated in the opposite direction. The tensile wave and the compression wave were superimposed. If the superimposed wave was a tensile wave, and the peak was greater than dynamic tensile strength of the steel-fiber concrete, the tensile cracks were produced in the corresponding areas, which was the spall pit. When the subsequent superimposed wave peak was less than the dynamic tensile strength, the spall damage no longer occurred, and the size and shape of the spall pit remained unchanged.

4.2 Damage Analyses

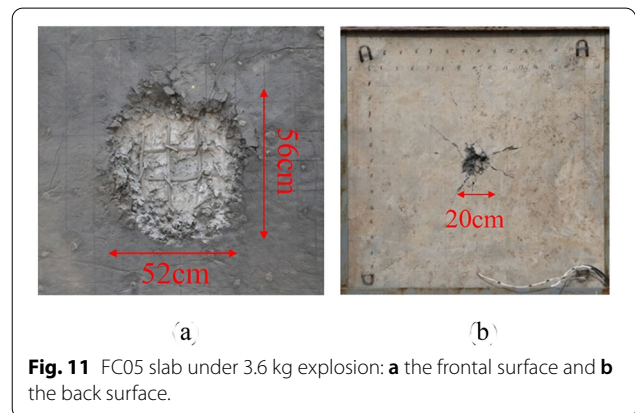
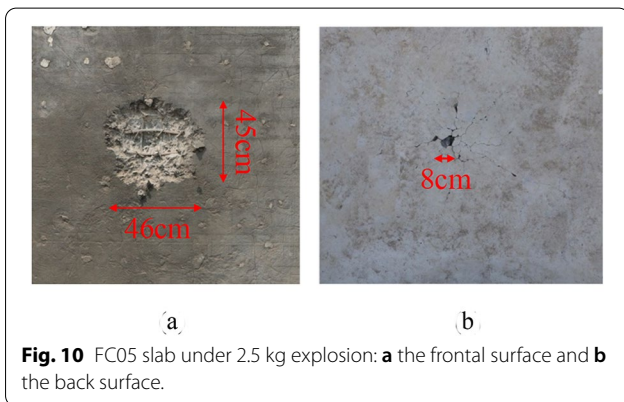
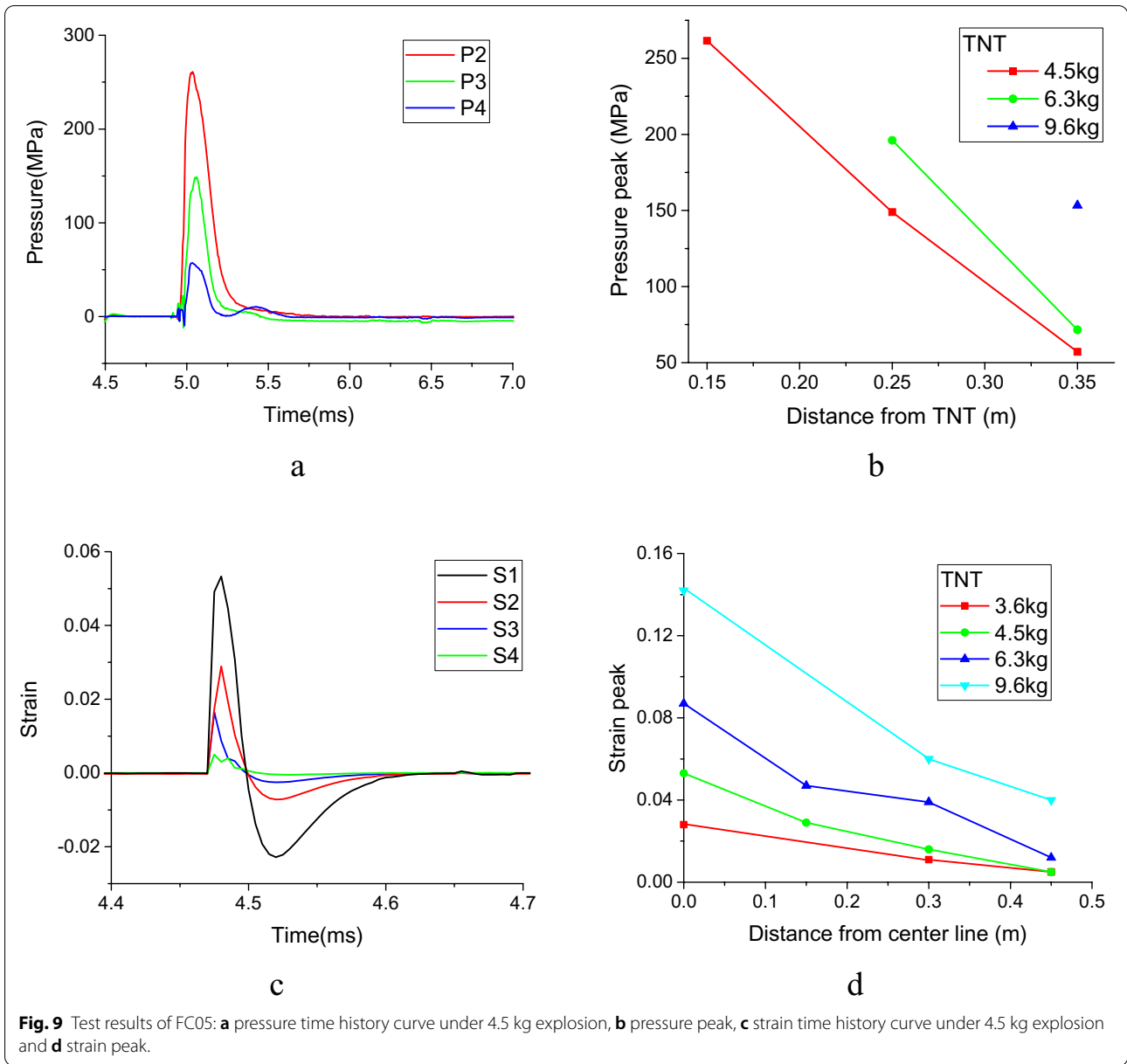
Through systematic analysis of the explosion test results of the FC05 slab, it can be found that under the action of contact explosion, the following typical failure modes occur in the steel-fiber reinforced concrete slabs.

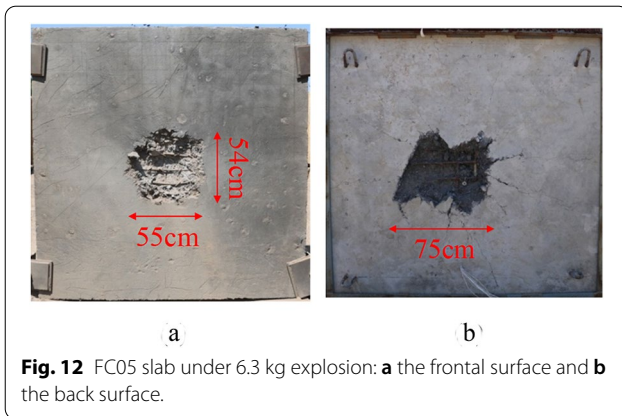
4.2.1 Minor Damage Mode

When the charge is 2.5 kg, the failure of the slab is minor damage mode, as shown in Fig. 10. There was a blasting crater on the frontal surface, and the area of blasting crater was $46 \text{ cm} \times 45 \text{ cm}$, and the depth was 8.5 cm. The steel was exposed, but it was not blown up. There were few cracks around the crater. The back surface of the slab was bulged, the bulged area was round, and the height was 1.5 cm. There were radical cracks from the projection point, and the width of cracks was less than 0.5 mm. Real sound was heard on the surface by hammering.

4.2.2 Minor Spall Mode

When the charge is $< 3.6 \text{ kg}$, the failure of the slab is minor spall mode, as shown in Fig. 11. The area and depth of the blasting crater were increased, and the crater shape was approximately circular but partially irregular. The steel was also exposed, but was not blown up. The size of the blasting crater was significantly larger than that of the spall pit. The spall pit was small in size, with a diameter of 20 cm and a depth of 5 cm. Some steel-fiber





concrete fragments in the spall pit were peeled off, and no steel were exposed. There were 12 obvious radial cracks around the spall pit, with a width of 0.5–1 mm, and some more subtle cracks. The surface was heard empty sound by hammering.

4.2.3 Moderate Spall Mode

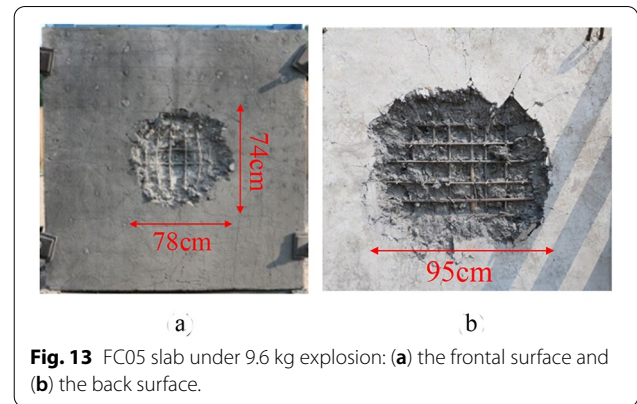
As the charge continues to increase, the slab exhibits moderate spall damage. The damage of FC05 slab under 6.3 kg explosion can be shown in Fig. 12. The area and depth of blasting crater continued to increase. The area was 54 cm × 55 cm, and the depth was 10.5 cm. The number of exposed steels increased, but none of them broke. The size of the blasting crater was smaller than that of the spall pit. The diameter and depth of spall pit have changed to 75 cm and 13 cm, respectively. Most of the concrete fragments in the spall pit were peeled off, and the steel bars were not broken, but exposed. There were more than 10 obvious radial cracks around the spall pit, whose depth were 0.5 mm to 2 mm.

4.2.4 Severe Spall Mode

When subjected to 9.6 kg explosion, FC05 slab was severely spalled, as shown in Fig. 13. The size of blasting crater was significantly enlarged, and there were 2 steel bars broken in the crater. The size of spall pit was significantly larger than blasting crater. The diameter and depth of the spall pit of the back surface were large, the fragments flew away at high speed, some steel bars were exposed, and there were obvious cracks around the spall pit, extending to the four sides of the slab.

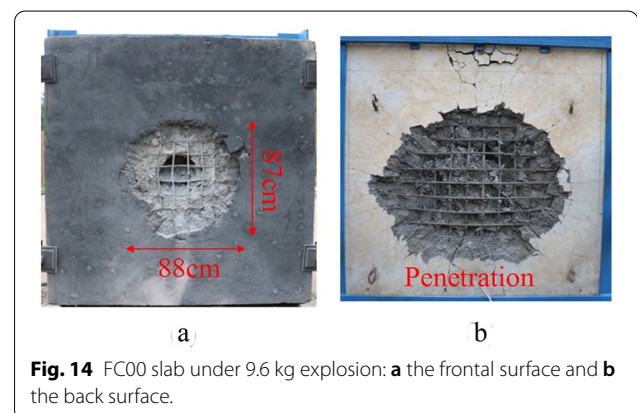
4.2.5 Penetration Mode

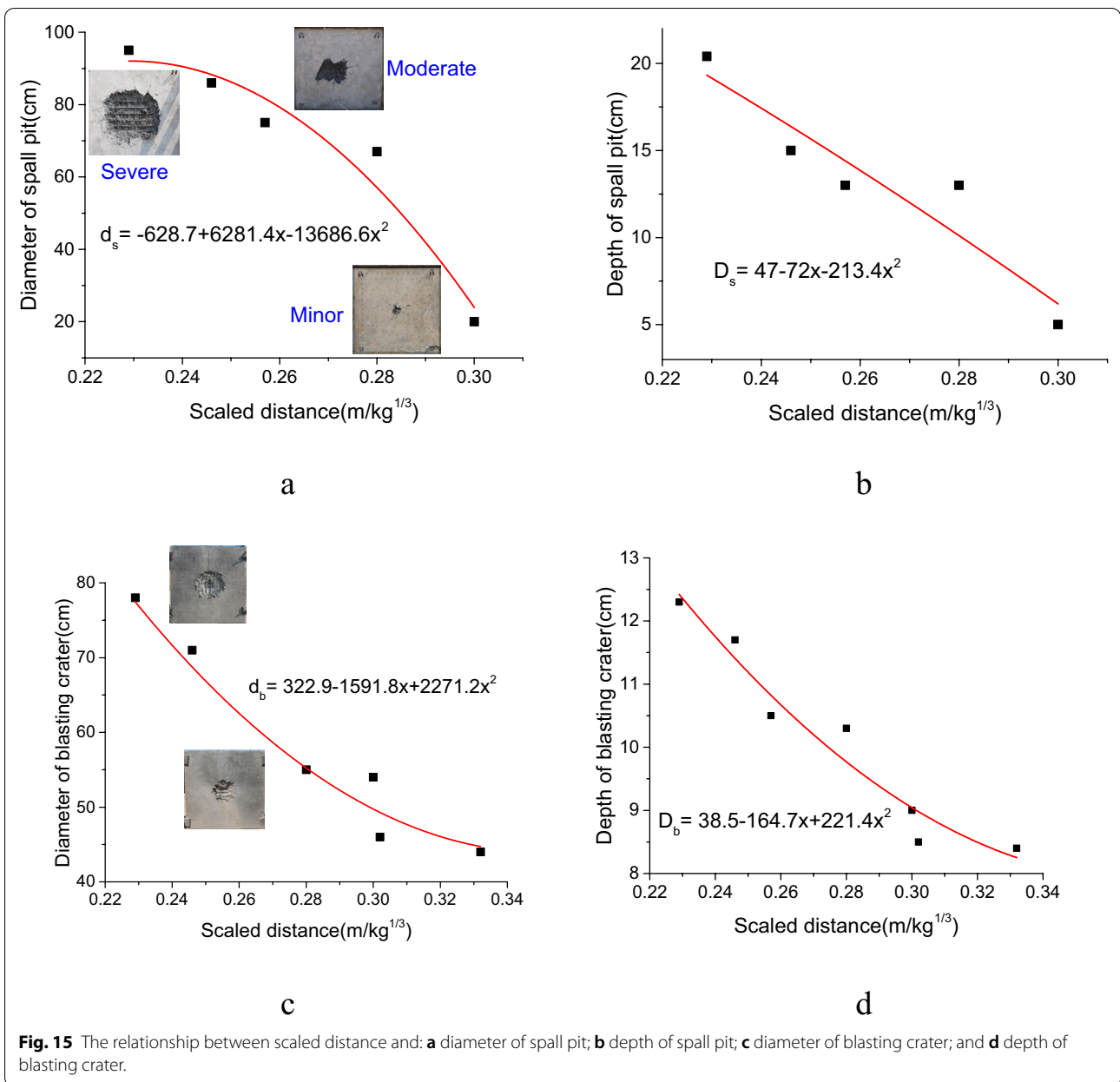
It can be expected that as the charge continues to increase, the slab will have a penetrating phenomenon, that is, the slab will have a blasting crater on the frontal face, and a spall pit will be formed on the back surface,



and the two will penetrate each other. As shown in Fig. 14, common reinforced concrete slab FC00 has penetrating damage under the action of 9.6 kg explosion. The size of blasting crater and spall pit were large, the steel bars were exposed and some were broken, and the cracks were many and wide, extending to the periphery.

The relationship between scaled distance x and damage of slabs is summarized in Fig. 15. It can be found that with the decreasing of scaled distance, the damage degree of blasting crater and spall pit increases. From minor damage to moderate damage, the diameter of spall pit enlarges rapidly, while from moderate damage to severe damage, the increase rate of diameter is slow, which reflects that the spall resistance of steel-fiber reinforced concrete has become more obvious. Subjected to contact explosion, the diameter and depth of the blasting crater increase obviously with the increase of the TNT, and the damage degree becomes larger and larger. It is difficult to find that the structure has obvious anti-blast performance.





4.3 Fragments of Concrete

Subjected to the explosion loading, the steel-fiber reinforced concrete slab is spalled, causing a large number of fragments on the back surface to fly out, as shown in Fig. 16. Analysis of the distribution law of fragments can provide a basis for the application of steel-fiber reinforced concrete slabs in protective structures. The definition of horizontal distribution angle is shown in Fig. 17. Taking the midpoint of the bottom end of the slab as the origin, the angle between the fragment on the ground and the y -axis is the horizontal distribution angle θ . The maximum horizontal distribution

angle θ_{\max} of the spalled fragments is shown in Fig. 18a. As the charge increases, that is, the scaled distance decreases, the maximum horizontal distribution angle increases approximately linearly. The fitted curve of the relationship between θ_{\max} and the scaled distance x can be expressed as

$$\theta_{\max} = 75 - 214x. \tag{8}$$

According to the statistical results of the spalled fragments under the explosion of different charges, the mass distribution of the fragments along the y -axis can be



Fig. 16 Test site fragment distribution map.

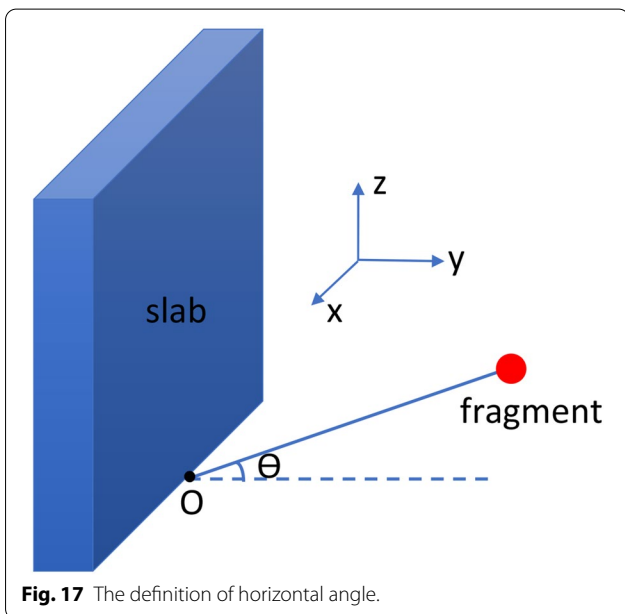


Fig. 17 The definition of horizontal angle.

seen. Figure 18b shows the relationship between fragment percentage and distance of FC05 slab. Each point in this graph represents the sum of the mass fractions falling within a certain distance from the back surface of the slab. Since the bamboo frame is 20 m away from the slab, the mass percentage must be 100% at 20 m. As the charge increases, the throwing speed of the fragments is significantly accelerated, and the number of fragments located further away increases. When the charge is 9.6 kg, some of the fragments are inserted into the bamboo frame due to the impact force.

4.4 Effect of Steel-Fiber on Spall Resistance

The size and depth of the blasting crater and spall pit produced by the above-mentioned 37 explosion tests are shown in Table 5. Compared with ordinary reinforced concrete, steel-fiber reinforced concrete has very good spall resistance. From this table, the effect of steel fiber on spall resistance can be found.

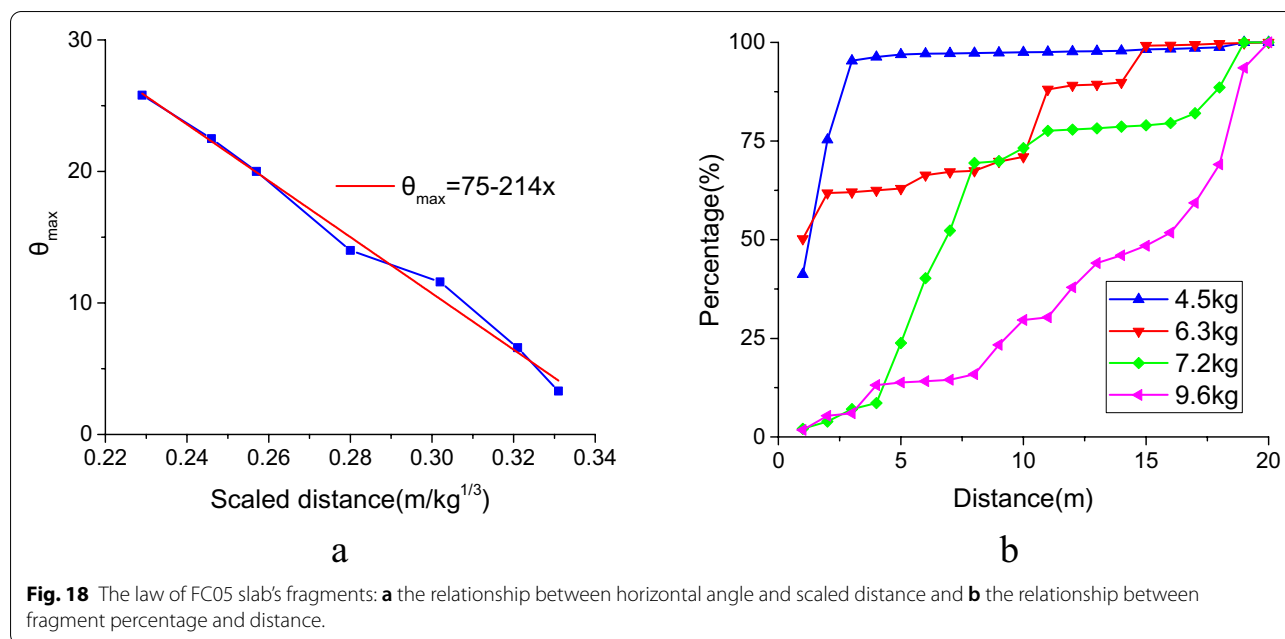
It can be predicted that as the scaled distance decreases, the damage of the spall pit becomes more serious. The effect of steel-fiber shape on the spall resistance is shown in Fig. 19. When the length, length–diameter ratio and volume percentage of steel fiber are the same, the slab of the hook-end steel fiber has the strongest spall resistance, and the diameter and depth of the spall pit are the smallest. The corrugated and dumbbell-shaped steel fibers have different effects on diameter and depth of spall pit. The effect of corrugated steel fiber on the depth is more obvious, and the effect of dumbbell steel fiber on the diameter is greater.

The effect of length on spall resistance can be shown in Fig. 20. When scaled distance is $0.302 \text{ m/kg}^{1/3}$, there is almost no difference in the effect of length. However, as the scaled distance decreases, the effect of steel-fiber length is prominent. When the steel-fiber length is 30 mm, the spall resistance of slab is the best. It shows that the increase of steel-fiber length has no obvious advantage to its spall resistance.

The effect of length–diameter ratio on spall resistance can be shown in Fig. 21. It is obvious that the larger the length–diameter ratio is, the smaller the diameter and depth of spall pit is, indicating that the better the spall resistance.

The effect of steel-fiber volume percentage on spall resistance can be shown in Fig. 22. It can be seen that the more volume percentage of steel fiber is, the better the anti-spall performance is. However, as the volume percentage increases, the advantage of improvement is not obvious any more.

According to the above analysis, it can be found that, in order to improve the spall resistance within a reasonable range, the steel fiber should adopt the hook-end shape, increase the length–diameter ratio, and increase the volume percentage appropriately. The effect of length on the spall resistance is related to the scaled distance, which requires specific analysis. In this study, when the steel fiber adopts a hook-end shape with a length of 30 mm, a length–diameter ratio of 80, and a volume percentage of 3%, the anti-spall performance is the best.



5 Conclusions

The static characteristics of steel-fiber concrete were revealed by compressive test and splitting tensile test of steel-fiber concrete specimens. Through the contact explosion test of steel-fiber reinforced concrete slab, the anti-spall performance of steel-fiber reinforced concrete was analyzed. It is concluded that:

- (1) Steel fibers have different effects on the compressive and splitting tensile strength of concrete. Relatively speaking, the influence of steel fiber on compressive strength is not obvious. The hook-end steel fiber has the best splitting tensile strength. When the steel fiber with short length and large length–diameter ratio is selected and the volume percentage is increased, the splitting tensile strength of concrete increases significantly.
- (2) Steel-fiber reinforced concrete slabs have good resistance to spall and show five typical failure

modes under the action of blast loads. The maximum horizontal angle of the fragments generated by the impact is proportional to the scaled distance. The smaller the scaled distance is, the farther the fragments are located.

- (3) The influence of steel fiber on spall resistance is mainly reflected in the diameter and depth of the spall pit. The hook-end steel fiber has the most obvious anti-spall effect. When the length of the steel fiber decreases, the length–diameter ratio increases, and the volume percentage of the steel fiber increases, the spall resistance of the slab can be improved significantly.

The research on the static performance of steel-fiber concrete and the dynamic response of steel-fiber reinforced concrete slabs under blast loading provides a powerful test basis for the application of steel fiber concrete in protective engineering.

Table 5 The damage of slabs.

Working condition	Parameters of TNT		Blasting crater		Spall pit	
	Charge (kg)	Scaled distance (m/ kg ^{1/3})	Diameter (cm)	Depth (cm)	Diameter (cm)	Depth (cm)
FC00	3.6	0.300	60.0	12.5	90.0	8.0
	6.3	0.257	60.0	14.0	95.0	17.0
	9.6	0.229	88.0	Penetration	113.0	Penetration
FC01	3.6	0.300	45.0	8.5	50.0	5.0
	6.3	0.257	50.0	11.0	69.0	9.7
	9.6	0.229	69.0	13.5	72.0	14.0
FC02	3.6	0.300	56.0	9.5	80.0	7.0
	6.3	0.257	60.0	10.5	94.0	11.0
	9.6	0.229	78.0	13.7	100.0	15
FC03	3.6	0.300	53.0	9.5	73.0	7.5
	6.3	0.257	60.0	10.9	77.0	17.0
	9.6	0.229	76.0	13.2	96.0	19.0
FC05	2.5	0.332	44.0	8.4	Bulge	
	3.0	0.302	46.0	8.5	Bulge	
	3.6	0.300	54.0	9.0	20.0	5.0
	4.5	0.280	55.0	10.3	67.0	13.0
	6.3	0.257	55.0	10.5	75.0	13.0
	7.2	0.246	71.0	11.7	86.0	15.0
	9.6	0.229	78.0	12.3	95.0	20.4
FC06	3.6	0.300	57.0	8.0	20.0	5.0
	6.3	0.257	60.0	11.0	80.0	15.0
	9.6	0.229	75.0	14.0	98.0	18.6
FC07	3.6	0.300	50.0	9.0	94.0	8.7
	6.3	0.257	53.0	11.0	82.0	15.0
	9.6	0.229	76.0	13.5	102.0	17.0
FC09	3.6	0.300	49.0	9.2	15.0	–
	6.3	0.257	55.0	11.0	60.0	5.8
	9.6	0.229	72.0	12.7	90.0	13.0
FC10	3.6	0.300	48.0	10.0	85.0	–
	6.3	0.257	60.0	10.5	90.0	14.0
	9.6	0.229	70.0	13.0	96.0	17.5.0
FC11	3.6	0.300	50.0	8.5	72.0	–
	6.3	0.257	57.0	10.5	74.0	9.5
	9.6	0.229	80.0	13.0	95.0	13.0
FC12	3.6	0.300	47.0	8.8	66.0	–
	6.3	0.257	62.0	11.0	70.0	8.5
	9.6	0.229	71.0	12.0	93.0	10.5

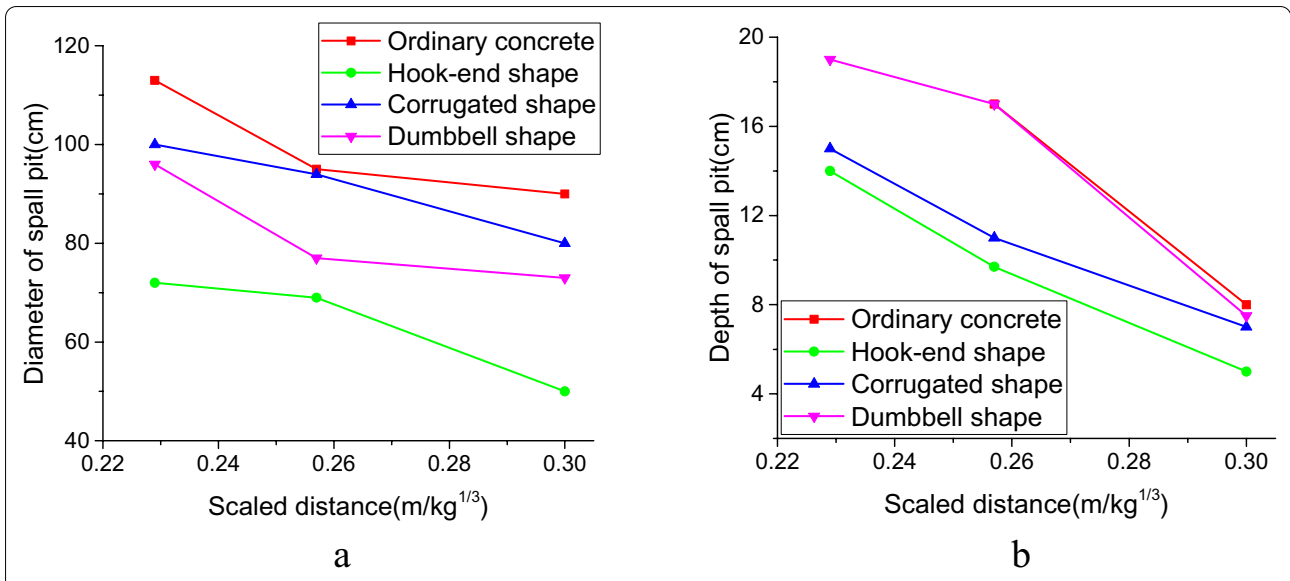


Fig. 19 The effect of the steel-fiber shape: **a** diameter and **b** depth of the spall pit.

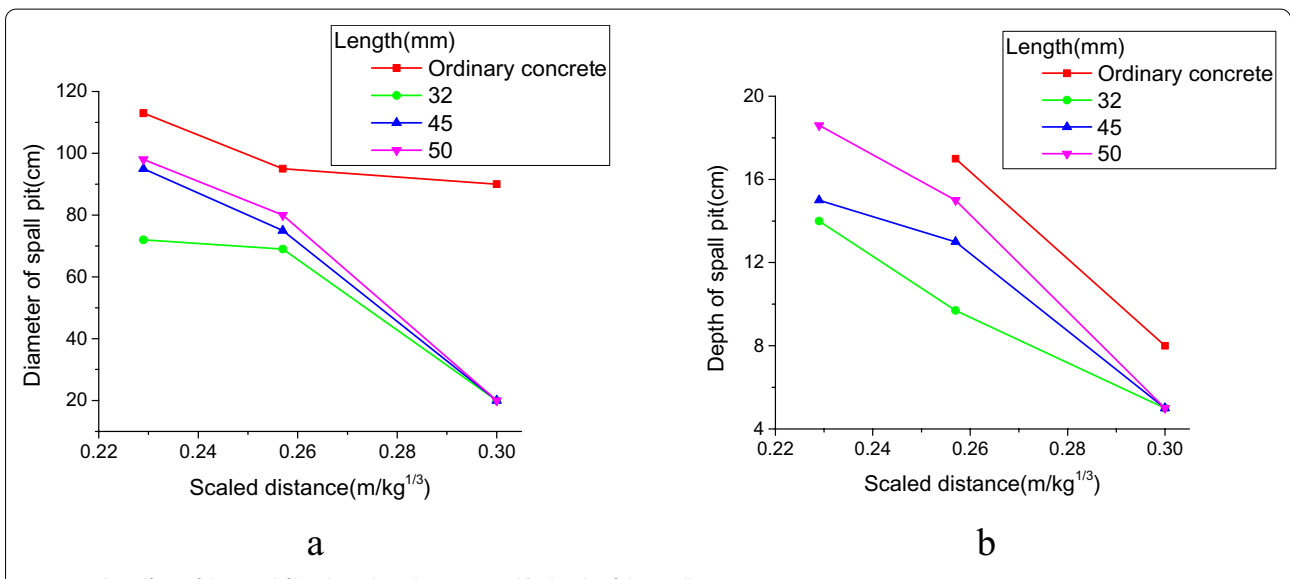
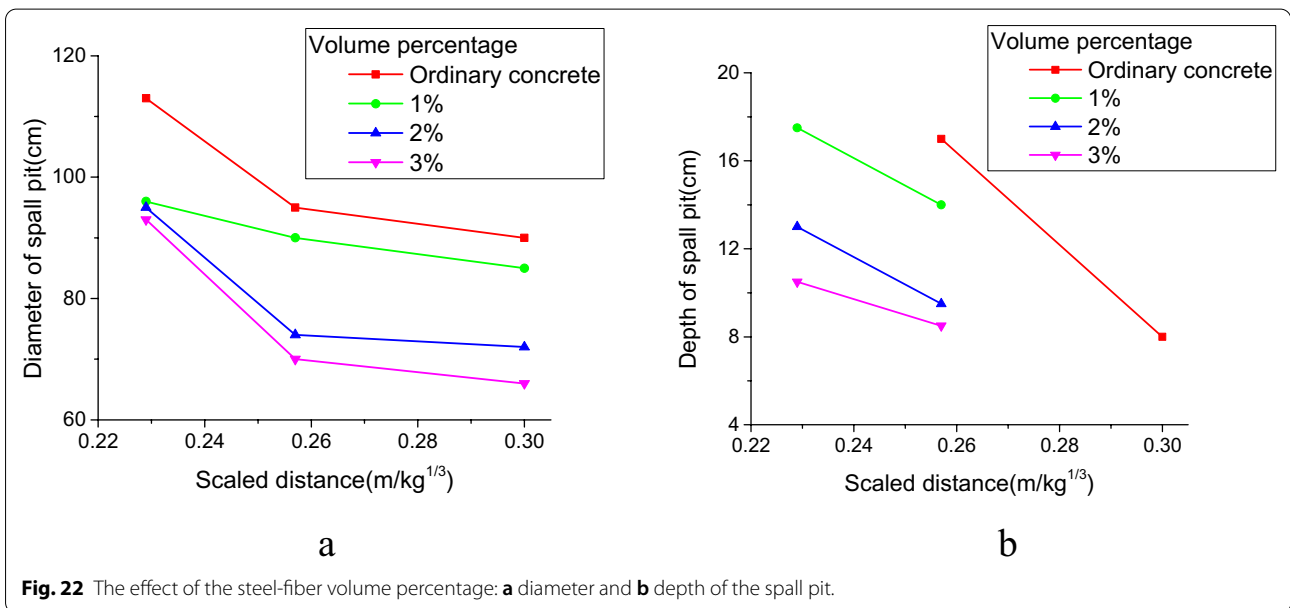
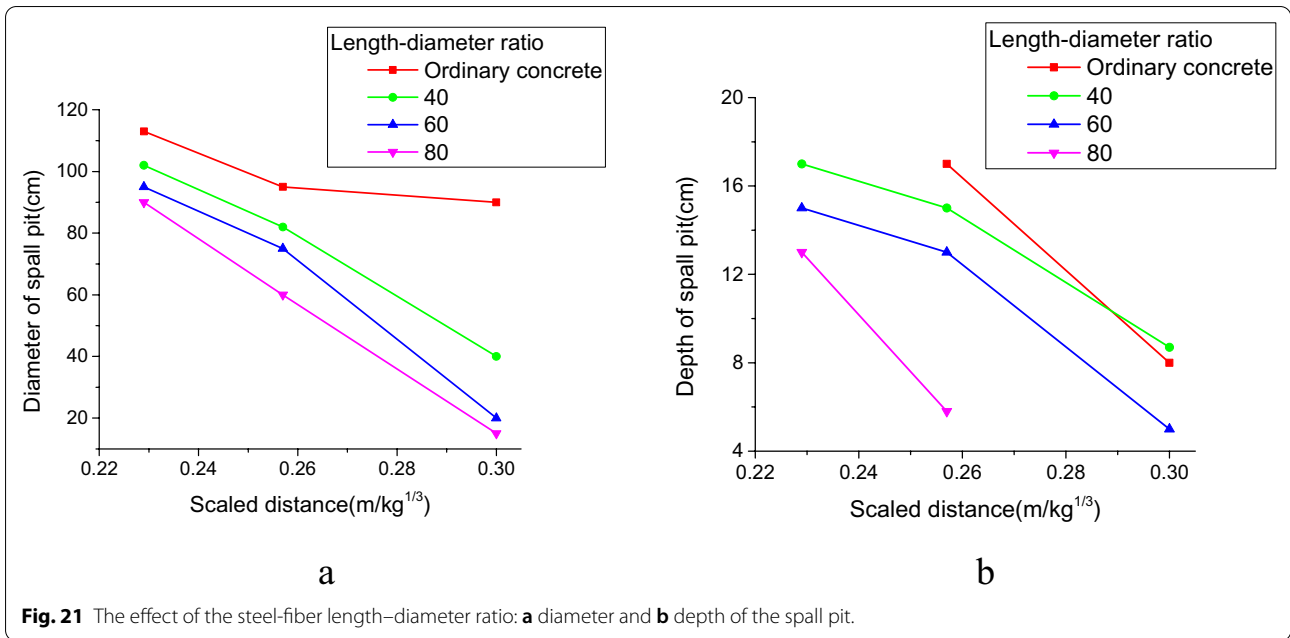
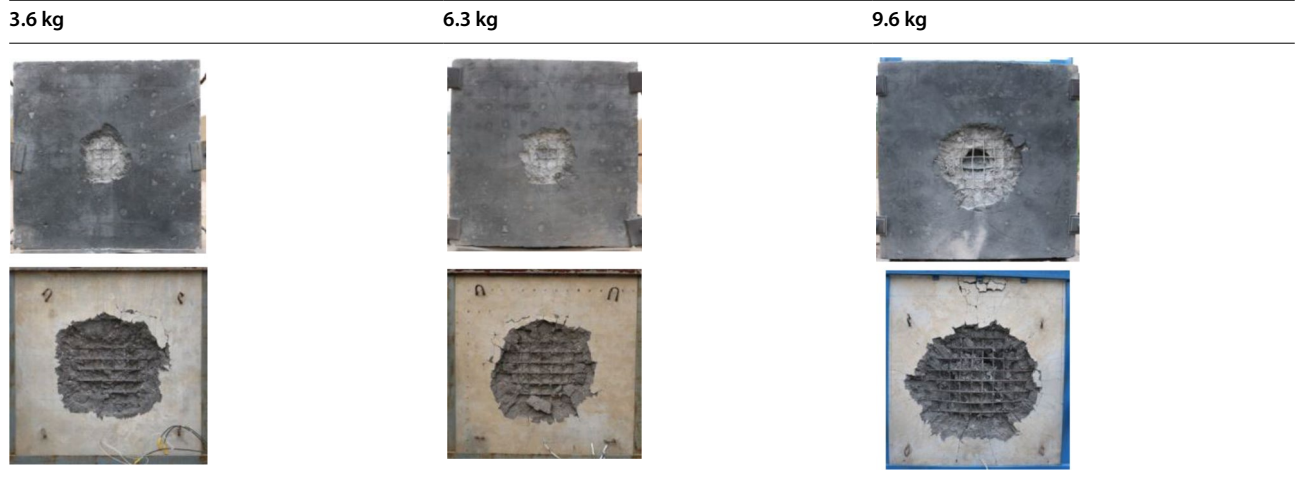


Fig. 20 The effect of the steel-fiber length: **a** diameter and **b** depth of the spall pit.

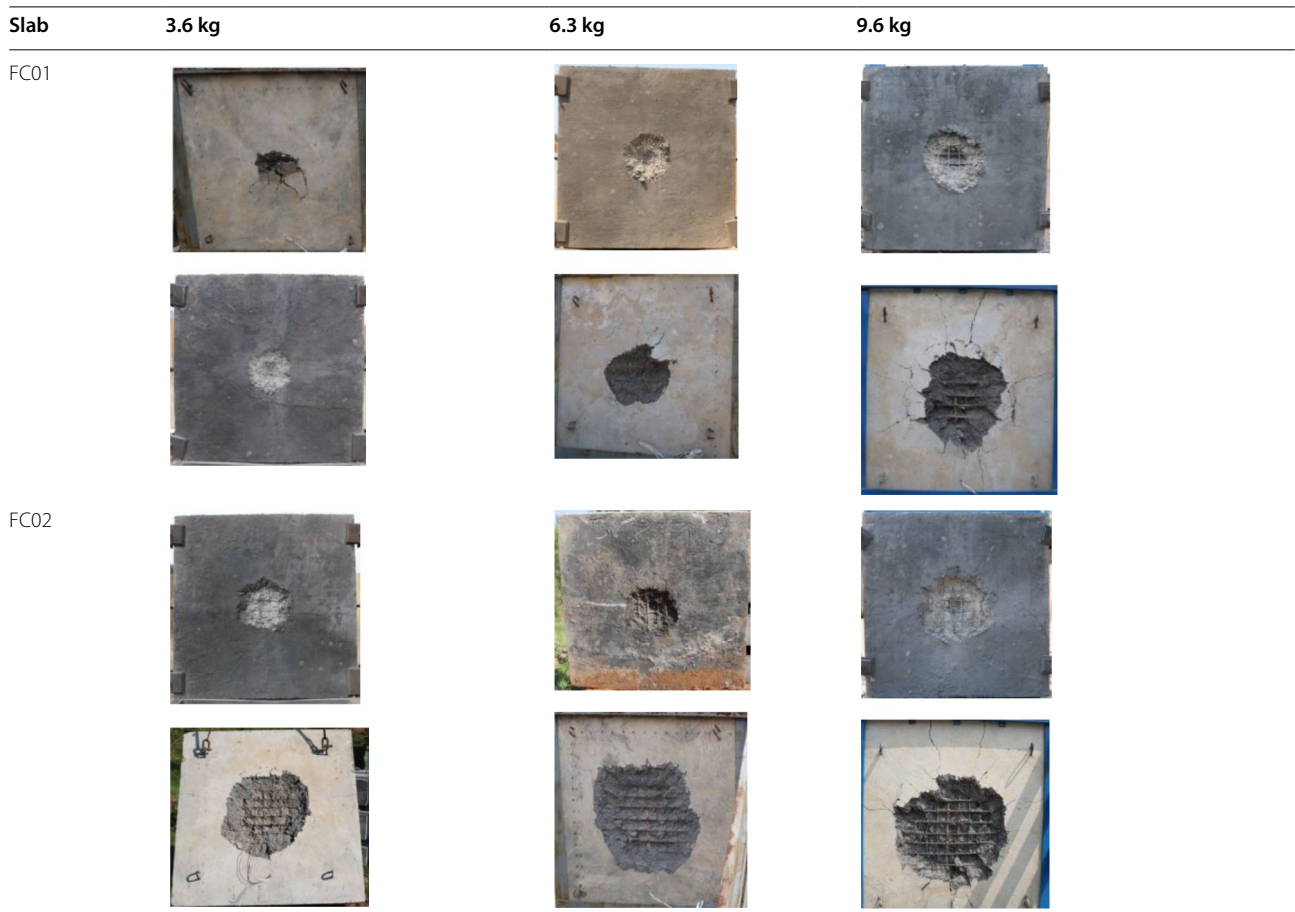


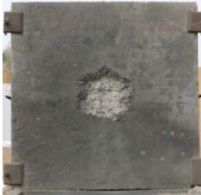





Appendix

(1) FC00 slab.



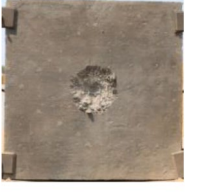











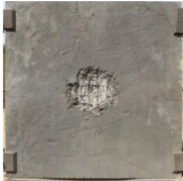


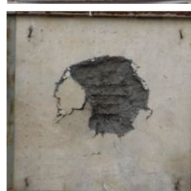


(2) Test results of shape comparison.















Slab	3.6 kg	6.3 kg	9.6 kg
FC03	 	 	 







(3) Test results of length comparison.

Slab	3.6 kg	6.3 kg	9.6 kg
FC04	 	 	 
FC05	 	 	 

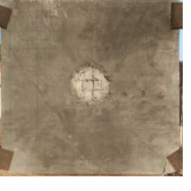







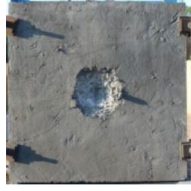



Slab	3.6 kg	6.3 kg	9.6 kg
FC06	 	 	 

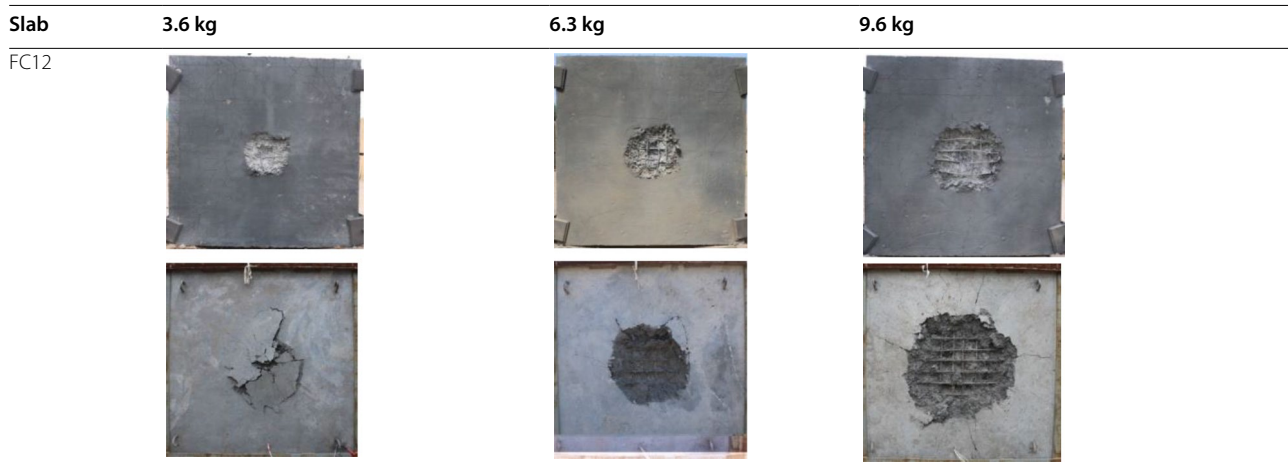
(4) Test results of length–diameter ratio comparison.

Slab	3.6 kg	6.3 kg	9.6 kg
FC07	 	 	 
FC08	 	 	 

Slab	3.6 kg	6.3 kg	9.6 kg
FC09	 	 	 

(5) Test results of volume percentage comparison.

Slab	3.6 kg	6.3 kg	9.6 kg
FC10	 	 	 
FC11	 	 	 



Acknowledgements

Supports from National Natural Science Foundation of China (51908549) are gratefully acknowledged.

Authors' contributions

DY is mainly responsible for completing the first draft of the article and participating in the experiment. GL is responsible for coordinating and arranging the progress of the entire experiment. BZ is responsible for the overall and content modification of the article. All authors read and approved the final manuscript.

Funding

This research was funded by the National Natural Science Foundation of China (NSFC) under Grant numbers 51908549.

Availability of data and materials

The authors confirm that the data are available within the article and its supplementary materials.

Declarations

Competing interests

The authors declare that they have no competing interests.

Authors' information

Bei Zhang is an assistant researcher, Dapeng Yang is an engineer, and Liu Guojun is an associate researcher.

Author details

¹Institute of Defense Engineering, AMS, PLA, Luoyang 471023, China. ²Institute of Defense Engineering, AMS, PLA, Beijing 100850, China.

Received: 1 December 2020 Accepted: 30 March 2021

Published online: 30 April 2021

References

- Aoude, H., Dagenais, F. P., Burrell, R. P., et al. (2015). Behavior of ultra-high performance fiber reinforced concrete columns under blast loading. *International Journal of Impact Engineering*, *80*, 185–202.
- Behbahani HP, Nematollahi B. Steel fiber reinforced concrete: A review 2011.
- Burrell, R. P., Aoude, H., & Saatcioglu, M. (2014). Response of SFRC columns under blast loads. *Journal of Structural Engineering*, *141*(9), 04014209.
- Chanh, N. V. (2017). *Steel fiber reinforced concrete*. Singapore: Springer Singapore.
- Chen, H. L., Xie, W., Jiang, M. R., et al. (2015). Blast-loaded behaviors of severely damaged buried arch repaired by anchored CFRP strips. *Composite Structures*, *122*, 92–103.
- Chen, H. L., Zhou, J. N., Fan, H. L., et al. (2014). Dynamic responses of buried arch structure subjected to subsurface localized impulsive loading: Experimental study. *International Journal of Impact Engineering*, *65*, 89–101.
- Fang, Q., & Zhang, J. (2013). Three-dimensional modelling of steel fiber reinforced concrete material under intense dynamic loading. *Construction and Building Materials*, *44*(7), 118–132.
- Feng, J., Zhou, Y. Z., Wang, P., et al. (2017). Experimental research on blast-resistance of one-way concrete slabs reinforced by BFRP bars under close-in explosion. *Engineering Structures*, *150*, 550–561.
- Gunaryo, K., Heriana, H., Sitompul, MR., et al. (2020) Experimentation and numerical modeling on the response of woven glass/epoxy composite plate under blast impact loading. *International Journal of Mechanical and Materials Engineering*, *15*(1).
- Han, D., Park, Y. J., Han, M. C., et al. (2019). Evaluation on protection performance and on-site applicability of hybrid fiber-reinforced concrete. *International Journal of Concrete Structures and Materials*, *13*(1), 19.
- Jahami, A., Temsah, Y., & Khatib, J. (2019). The efficiency of using CFRP as a strengthening technique for reinforced concrete beams subjected to blast loading. *International Journal of Advanced Structural Engineering*, *11*, 411–420.
- Lee, D. H., Han, S. J., Kim, K. S., et al. (2017). Shear capacity of steel fiber-reinforced concrete beams. *Structural Concrete*, *18*(2), 278–291.
- Li, J., Wu, C., Hao, H., et al. (2015a). Investigation of ultra-high performance concrete under static and blast loads. *International Journal of Protective Structures*, *6*(2), 217–235.
- Li, J., Wu, C., & Hao, H. (2015b). An experimental and numerical study of reinforced ultra-high performance concrete slabs under blast loads. *Materials and Design*, *82*, 64–76.
- Li, J., Wu, C., Hao, H., et al. (2016). Experimental investigation of ultra-high performance concrete slabs under contact explosions. *International Journal of Impact Engineering*, *93*, 62–75.
- Li, J., Wu, C., Hao, H., et al. (2017). A study of concrete slabs with steel wire mesh reinforcement under close-in explosive loads. *International Journal of Impact Engineering*, *110*, 242–254.
- Li, N., Zhao, J. H., Li, Y., et al. (2014). Study on failure mode of steel fiber reinforced high strength concrete wall under blasting load. *Advanced Materials Research*, *1030–1032*, 1014–1018.
- Liu, S. F., Zhou, Y. Z., Zheng, Q., et al. (2019). Blast responses of concrete beams reinforced with steel-GFRP composite bars. *Structures*, *22*, 200–212.
- Luccioni, B., Isla, F., Codina, R., et al. (2017). Effect of steel fibers on static and blast response of high strength concrete. *International Journal of Impact Engineering*, *107*, 23–37.
- Mao, L., Bamett, S., Begg, D., et al. (2014). Numerical simulation of ultra high performance fiber reinforced concrete panel subjected to blast loading. *International Journal of Impact Engineering*, *64*(64), 91–100.
- Michels, J., Christen, R., & Waldmann, D. (2013). Experimental and numerical investigation on postcracking behavior of steel fiber reinforced concrete. *Engineering Fracture Mechanics*, *98*, 326–349.
- Nam, J., Kim, H., & Kim, G. (2017). Experimental investigation on the blast resistance of fiber-reinforced cementitious composite panels subjected to

- contact explosions. *International Journal of Concrete Structures and Materials*, 11(1), 29–43.
- Nataraja, M. C., Dhang, N., & Gupta, A. P. (1999). Stress–strain curves for steel-fiber reinforced concrete under compression. *Cement and Concrete Composites*, 21(5–6), 383–390.
- Porter, H. F. (1910). The preparation of concrete—from selection of materials to final deposition. *Journal Proceedings of American Concrete Institute*, 6(2), 296.
- Pros, A., Díez, P., & Molins, C. (2012). Modeling steel fiber reinforced concrete: numerical immersed boundary approach and a phenomenological meso-model for concrete-fiber interaction. *International Journal for Numerical Methods in Engineering*, 90(1), 65–86.
- Rambo, D. A. S., Silva, F. D. A., & Filho, R. D. T. (2014). Mechanical behavior of hybrid steel-fiber self-consolidating concrete: Materials and structural aspects. *Materials and Design*, 54(2), 32–42.
- Saboori, A., Yazdani, S., Reberg, A., et al. (1976). Steel fiber reinforced concrete. *Materials Science and Engineering*, 25, 53–58.
- Thomas, J., & Ramaswamy, A. (2007). Mechanical properties of steel fiber-reinforced concrete. *Journal of Materials in Civil Engineering*, 19(5), 385–392.
- Tokgoz, S., & Dundar, C. (2010). Experimental study on steel tubular columns in-filled with plain and steel fiber reinforced concrete. *Thin-Walled Structures*, 48(6), 414–422.
- Uygunoğlu, T. (2008). Investigation of microstructure and flexural behavior of steel-fiber reinforced concrete. *Materials and Structures*, 41(8), 1441–1449.
- Wanchoo, P., Matos, H., Rousseau, C. E., et al. (2021). Investigations on air and underwater blast mitigation in polymeric composite structures—a review. *Composite Structures*, 263, 113530.
- Wang, H. H., Chen, H. L., Wang, P., et al. (2019). Blast responses and damage evaluation of CFRP tubular arches. *Construction and Building Materials*, 196, 233–244.
- Wang, P., Jiang, M. R., Zhou, J. N., et al. (2018). Spalling in concrete arches subjected to shock wave and CFRP strengthening effect. *Tunneling and Underground Space Technology*, 74, 10–19.
- Xie, W., Jiang, M. R., Chen, H. L., et al. (2014). Experimental behaviors of CFRP cloth strengthened buried arch structure subjected to subsurface localized explosion. *Composite Structures*, 116, 562–570.
- Xu, J., Wu, C., Xiang, H., et al. (2016). Behaviour of ultra high performance fiber reinforced concrete columns subjected to blast loading. *Engineering Structures*, 118, 97–107.
- Yang, J. M., Yoo, D. Y., You-Chan, K., et al. (2017). Mechanical properties of steam cured high-strength steel fiber-reinforced concrete with high-volume blast furnace slag. *International Journal of Concrete Structures and Materials*, 11(2), 391–401.
- Yi, N. H., Kim, J. H. J., Han, T. S., et al. (2012). Blast-resistant characteristics of ultra-high strength concrete and reactive powder concrete. *Construction and Building Materials*, 28(1), 694–707.
- Yoo, D. Y., & Yoon, Y. S. (2016). A review on structural behavior, design, and application of ultra-high-performance fiber-reinforced concrete. *International Journal of Concrete Structures and Materials*, 10(2), 125–142.
- Zhang, B., He, H. G., Zhou, Q., et al. (2019). Blast responses of pultruded GFRP fluted-core sandwich panels: Testing and analyzing. *Polymer Testing*, 79, 106047.
- Zhang, N., Zhou, J., & Ma, G. W. (2020). Dynamic properties of strain-hardening cementitious composite reinforced with basalt and steel fibers. *International Journal of Concrete Structures and Materials*, 14(1), 44.
- Zhao, Z., Zhang, B., Zhou, J., et al. (2018). Quasi-far-field blast responses of hierarchical orthogrid-stiffened sheet molding compound (SMC) protective door structures. *Engineering Structures*, 168, 431–446.

Publisher's Note

Springer Nature remains neutral with regard to jurisdictional claims in published maps and institutional affiliations.

Submit your manuscript to a SpringerOpen® journal and benefit from:

- Convenient online submission
- Rigorous peer review
- Open access: articles freely available online
- High visibility within the field
- Retaining the copyright to your article

Submit your next manuscript at ► [springeropen.com](https://www.springeropen.com)
